HHS Public Access

Author manuscript

IEEE Trans Biomed Eng. Author manuscript; available in PMC 2015 September 01.

Published in final edited form as:

IEEE Trans Biomed Eng. 2014 November ; 61(11): 2779–2786. doi:10.1109/TBME.2014.2329461.

Toward Microendoscopic Electrical Impedance Tomography for Intraoperative Surgical Margin Assessment

Ryan J. Halter* **[Member, IEEE]** and

Thayer School of Engineering and Geisel School of Medicine, Dartmouth College, Hanover, NH 03755 USA.

Young-Joong Kim

Dartmouth College, Hanover, NH 03755 USA. He is now with Duke University, Durham, NC 27708 USA (yk91@duke.edu).

Abstract

No clinical protocols are routinely used to intraoperatively assess surgical margin status during prostate surgery. Instead, margins are evaluated through pathological assessment of the prostate *following* radical prostatectomy, when it is too late to provide additional surgical intervention. An intraoperative device potentially capable of assessing surgical margin status based on the electrical property contrast between benign and malignant prostate tissue has been developed. Specifically, a microendoscopic electrical impedance tomography (EIT) probe has been constructed to sense and image, at near millimeter resolution, the conductivity contrast within heterogeneous biological tissues with the goal of providing surgeons with real-time assessment of margin pathologies. This device consists of a ring of eight 0.6-mm diameter electrodes embedded in a 5-mm diameter probe tip to enable access through a 12-mm laparoscopic port. Experiments were performed to evaluate the volume of tissue sensed by the probe. The probe was also tested with inclusions in gelatin, as well as on a sample of porcine tissue with clearly defined regions of adipose and muscle. The probe's area of sensitivity consists of a circular area of 9.1 mm^2 and the maximum depth of sensitivity is approximately 1.5 mm. The probe is able to distinguish between high contrast muscle and adipose tissue on a sub-mm scale (~500 μm). These preliminary results suggest that EIT is possible in a probe designed to fit within a 12-mm laparoscopic access port.

Keywords

Electrical impedance tomography (EIT); prostate cancer; radical prostatectomy (RP); surgical margin assessment

I. Introduction

Prostate cancer is the most diagnosed form of cancer and the second leading cause of cancer-related death in men. In 2014, 27% (233 000 men) of all diagnosed cancers are expected to be within the prostate and approximately 29 480 men are expected to die as a

* (ryan.j.halter@dartmouth.edu).

Authors' photographs and biographies not available at the time of publication.

result of the disease [1]. The detection of prostate cancer has matured since prostate specific antigen (PSA)-testing began and as a result, the PSA-era in the United States has witnessed the number of prostate cancers diagnosed increase from 96.1 to 177.8 per 100 000 men since 1974 [2] with a larger portion of these men having localized disease. This has lead to a significant increase in the number of men undergoing radical curative therapies to address their disease with the CDC reporting that approximately 138 000 radical prostatectomies were performed in the USA in 2010 [3].

Radical prostatectomy (RP) aims to remove the prostate from the body with the objective of eradicating all cancer cells, maintaining urinary continence, and preserving erectile function. Following a routine RP, the prostate is pathologically assessed for tumor size, Gleason grade (level of tumor differentiation), extracapsular extension (ECE), seminal vesicle (SV) or vas deferens (VD) involvement, and positive surgical margins (PSMs). Patients with ECE and/or PSMs may be offered an immediate adjuvant therapy in the form of hormones and/or external beam radiation. If the pathological prognosis is good, these patients will have their PSA levels routinely monitored. Patients with biochemical recurrence, as indicated by high levels of PSA, are either put on watchful waiting or active surveillance strategies or offered salvage therapies of external beam radiation and/or hormonal therapy. These adjuvant or salvage therapies have adverse side-effects including proctitis, cystitis, irritable bowel syndrome, intermittent rectal bleeding, bladder irritability, and intermittent gross hematuria in the case of radiotherapy, and osteoporosis, hot flashes, sexual dysfunction, cognitive impairment, changes in body habitus, gynecomastia, and anemia in the case of hormonal therapy [4]. If all cancer cells are removed during RP, men have a high probability of a long disease-free survival and a low probability of biochemical recurrence, and as a result are not subjected to these noxious adjuvant and salvage therapies.

Patients with PSMs have a significantly increased risk of disease recurrence [5]–[7]. In one study, 18% of 3,478 men undergoing RP experienced cancer progression with ten-year biochemical progression-free survival estimates of 68%; patients with PSMs and ECE had a ten-year progression-free survival of only 53% [5]. Another group reported that 34% of patients with PSMs developed biochemical recurrence, while only 7.8% of those with negative surgical margins (NSMs) recurred; ten-year biochemical disease free survival for patients with PSMs was 59.9%, and for those with NSMs was 89.6% [6]. Similarly, in a large study of 5,831 men treated with RP, it was found that patients with PSMs had significantly higher progression rates than those with NSMs (36.1% versus 70.1% at ten years) [7]. In addition, when combined with other risk factors including ECE, SVI, lymph node involvement, pathological Gleason grade, and preoperative PSA, surgical margin status was still found to be an independent risk factor for biochemical recurrence [7].

Electrical impedance spectroscopy (EIS) gauges frequency-dependent electrical properties of tissue by applying small (<1 mA) alternating currents between two electrodes while recording resultant voltages forming across two other electrodes. The voltage-to-current ratio defines the electrical impedance, a function of tissue architecture that has been used to distinguish between normal and pathologic tissues in a variety of organs including cervix [8]–[11], breast [12]–[14], skin [15], [16], and bladder [17], [18]. Significantly different electrical property signatures have also been reported between malignant and benign

prostate [19]–[22]. These differences have been reported over the range of 100 Hz–1 MHz; additionally, parameterized spectral impedance parameters (derived from Cole-based parameterization [23]) have exhibited even more contrast with higher clinical metrics of sensitivity and specificity (approaching 70% and 81.5%, respectively) [21]. Electrical impedance tomography (EIT) is a method that uses EIS measurements across different sets of electrodes arranged in a known geometry in order to generate an image of the electrical properties of the tissue. If EIT could be intraoperatively used on the resected margins, images of the electrical properties of the tissue could provide surgeons with real-time feedback on the presence of PSMs and improve patient outcomes.

Today, the majority of radical prostatectomies in the US are being performed laparoscopically with robot assistance. To access the prostate through a laparoscopic port, the EIT probe must be both small enough to fit into the port and flexible enough to be maneuverable using robotic graspers (see Fig. 1). A probe that meets these specifications is described here. Specifically, an endoscopic device was developed to intraoperatively gauge these electrical properties and provide real-time pathological assessment of surgical margins. Several experiments are performed to evaluate the volume of tissue the probe senses as well as its capacity to detect changes in conductivity in a variety of geometries and environments.

II. Methods

A. Microendoscopic EIT Probe

The custom-designed EIT surgical margin assessment (EIT-SMA) probe consists of eight gold-plated copper electrodes arranged in a ring pattern and embedded into a 5-mm diameter polyethylene tip. The electrode assembly is housed within silicone tubing. The diameter of the silicone tubing is 7 mm, which is small enough to be inserted into a 12-mm diameter auxiliary port available during robot-assisted laparoscopic radical prostatectomy (RALP). The length of the tubing is ~55 cm which is of sufficient length for intracorporeal use during RALP; the length and elasticity of the silicone tubing provide the surgeon with sufficient dexterity to manipulate the probe so that it is capable of accessing all surgical surfaces. Each electrode has a diameter of 0.6 mm with the centers of opposite electrodes at a distance of 2.8 mm (see Fig. 2). It is this 2.8 mm diameter circle that forms the imaging field in the reconstructed EIT images. An eight-electrode ring pattern was chosen to enable 1) radially invariant image sensitivity, 2) high speed data acquisition (higher electrode numbers would require more data be recorded), and 3) data acquisition using EIT drive patterns optimized for circular domains. All materials can withstand temperatures of 135°C or higher, which enables the probe to be steam sterilized following routine sterilization protocols used at our institution (135°C steam sterilization for 6 min followed by a 45-min drying period).

The probe was interfaced to Dartmouth's voltage driven broadband EIT system [24]. This is a parallel 64-channel voltage driven system in which applied voltages and induced currents are sensed at each electrode. The system operates over a bandwidth of 10 kHz to 10 MHz and is programmed to record data at 20 logarithmically spaced frequencies. The acquisition bandwidth was limited to the nine logarithmically spaced frequencies spanning 10 kHz to 183 kHz because the effects of parasitic capacitances and inductances associated with the moderately long cables (~55 cm) are not able to be fully compensated with the calibration

procedure employed. The system was calibrated using the approach describe in [24]. Specifically, discrete loads were applied to each channel and a set of channel and frequency-dependent scaling factors was computed to ensure that the measured impedance reflected that of the known load impedance.

For this series of experiments, only eight of the system channels were used to interface with the eight-electrode probe. The system was configured to drive seven spatially variant trigonometric patterns [25], such that the applied voltages, *V*, followed the standard convention for these patterns:

$$V(p,e) = \begin{cases} cos\left(\frac{2\pi p(e-1)}{N_{elect}}\right) & p=1,2,3,4 \\ sin\left(\frac{2\pi p(e-1)}{N_{elect}}\right) & p=5,6,7 \end{cases} \quad (1)$$

where *p* is the pattern number (1, 2, . . . ,7), *e* is the electrode (1, 2, . . . ,8), and N_{elect} is the total number of electrodes (8 in this case). Trigonometric patterns have been shown to be the theoretically optimal patterns that can be applied for a circular domain [25]. Other spatial patterns, including driving signals between adjacent and opposite electrodes [26], are often used in EIT systems that make tetrapolar (four-electrode) based measurements. However, this probe was interfaced to a fully parallel drive/sense EIT system optimized for applying these multielectrode patterns. A full spectrum of EIT data (8 channels, 10 frequencies) was acquired in ~550 ms.

B. Image Reconstruction

Absolute conductivity images were computed using a dual-mesh finite element method based approach standard in EIT and described previously [27]. The forward problem was modeled using a two-dimensional (2-D) fine mesh consisting of 2560 triangular elements (1345 nodes) and the inverse problem was computed on a coarser mesh consisting on 640 triangular elements (353 nodes). Each mesh is a circular domain of diameter 2.8 mm. Electrodes were modeled as point-electrodes equiangularly spaced around the periphery of the mesh and the shunt-electrode model was used to describe the potential field and current density at the electrodes [28]. While more computationally complex three-dimensional image reconstruction is becoming the norm for certain EIT applications [29], [30], a 2-D approach was chosen here to speed image reconstruction computation as will ultimately be needed for clinical deployment; in *in vivo* use, this system will need to provide images in near real-time to enable surgeons to extract additional tissues as needed. Image reconstruction took <5 s to complete in MATLAB (Mathworks, Natick, MA) running on a 2.9 GHz Intel Core i7 processor.

C. Probe Evaluation

Phantom imaging studies were used to evaluate the probe in preparation for preclinical deployment. These studies include imaging saline phantoms, gelatin phantoms, and *ex vivo* porcine tissue.

1) Saline Phantoms—The probe was submerged in a saline bath to experimentally assess the probe tip's area of sensitivity (AOS) and the probe's maximum depth of sensitivity

(MDOS). Together, these metrics are used to describe the volume of tissue that influences the impedance measurements. The probe-tip's AOS is defined as the area below the probe–tissue interface (and parallel to the probe face) over which changes in tissue impedance result in detectable changes in the reconstructed conductivity image. The AOS includes the area directly under the probe, circumscribed by the electrode array, as well as the region outside the probe edge where fringing effects may occur and is reported in mm^2. Changes in tissue impedance outside of this area would not be detectable by the probe. Likewise, the MDOS describes the furthest distance from the probe–tissue interface (along the axial direction of the probe) at which point a change in impedance would no longer result in a detectable change in the reconstructed conductivity image; impedance changes beyond this depth would not be detectable by the probe.

The AOS and MDOS were both measured experimentally by inserting the probe in a tank filled with a saline solution (0.1 S/m) and translating the probe from the edge of a high impedance, nonconductive boundary preventing the flow of current (see Fig. 3). The EIT probe was submerged in the saline and mounted on a multiaxis optics stage such that the probe tip could be translated in both the axial and transverse directions at submillimeter increments. A piece of flat acrylic was used as a nonconducting surface with near-infinite impedance contrast with respect to the saline. For the MDOS test, the probe tip was moved from a position 0.5 mm in front of the acrylic to a distance of 10 mm away from the surface, with EIT measurements recorded at 500-μm intervals [see Fig. 3(a)]. For the AOS test, the edge of the electrode array was placed next to the acrylic slab and translated away from the interface at 250-μm steps to a total distance of 5 mm; EIT measurements were recorded at each step [see Fig. 3(b)]. Because of the electrode ring configuration used, the AOS will represent a circular area at the probe–tissue interface. For both AOS and MDOS experiments, conductivity images were generated at each step and the maximum conductivity of the image was evaluated. The distance at which the maximum conductivity of an image changes by less than 2% with respect to the image acquired at the previous step is used in defining the AOS and MDOS. In the case of the AOS experimental configuration, this distance represents the radius of the circular area. In the case of the MDOS configuration, this distance directly defines the MDOS. A threshold of 2% was chosen based on the typical image-to-image variation we observe during repeated data acquisitions.

2) Gelatin Phantoms—A high contrast metal wire inclusion (0.6-mm diameter) was embedded within a gelatin phantom to mimic how the probe would be used clinically (gelatin from porcine skin, Type A, G2500, Sigma-Aldrich, St. Louis, MO). This inclusion represents a near-infinite impedance contrast with respect to the gelatin and was used to verify that the probe was at least capable of imaging small regions of high contrast material in a heterogeneous imaging domain. The wire was positioned vertically within the gelatin slab and the EIT probe was positioned by hand over the wire inclusion in two different configurations; the wire was positioned at 3 o'clock and 9 o'clock positions. Data was collected from these two orientations and from a region on the gelatin in which no inclusion was present; this served as a blank homogenous sample.

3) Porcine Tissue—A heterogeneous sample of an *ex vivo* porcine tissue was used to demonstrate the probe's imaging capabilities in a biological setting. The tissue sample consisted of a large component of muscle surrounded by a rim of adipose tissue. In addition, strands of adipose tissues were present throughout the large muscle components. The EIT probe was first positioned at the muscle/adipose tissue interface and image data was recorded. The probe was rotated 180° and image data was recorded from 10 to 183 kHz. In a second experiment, the probe was positioned over a thin adipose streak, identified within the muscle, to explore the probe's ability to image smaller structures within a biological sample.

III. Results

A. Saline Phantoms

Conductivity maps were generated as the probe was moved away from the acrylic surface [as configured in Fig. 3(a)]. Fig. 4(a) shows the 2-D conductivity maps along with the conductivity profile at 127 kHz. The profile becomes constant after ~1.5 mm suggesting that the MDOS of the probe is 1.5 mm. The Gaussian conductivity distribution is a well-described phenomena associated with using a 2-D reconstruction algorithm to model a 3-D imaging domain [31]; specifically, the peripheral region of low conductivity surrounding the central peak is associated with the inherent point-spread function of EIT [26]. In addition, electrode artifacts (regions of low conductivity) associated with the point-electrode models used here are observed around the periphery of the images. The maximum conductivity was extracted from each 2-D conductivity map at six discrete frequencies (14.3 kHz, 29.7 kHz, 61.5 kHz, 127.4 kHz, 263.6 kHz, and 545.5 kHz) and plotted as a function of probe-acrylic distance [see Fig. 4(b)] to a maximum distance of 10 mm. These frequencies were chosen for display purposes only; all other system frequencies demonstrated similar trends. For all frequencies <200 kHz the maximum reconstructed conductivity reached a value of ~0.055 S/m, which was 45% less than the true conductivity of 0.1 S/m. This underestimation of conductivity is a common trend in absolute 2-D EIT imaging arising primarily from the assumed planar geometry. The maximum conductivity changed by less that 2% for all frequencies once the distance exceeded 1.5 mm, which is defined as the MDOS. The additional high frequency data (263.6 kHz and 545.5 kHz) is included to show how the unaccounted for parasitic impedances influence reconstructed conductivities; frequencies greater than 200 kHz will not be used in future *in vivo* deployment of this particular probe.

In terms of the probe-tip AOS, the maximum image conductivity varied by less than 2% for all step sizes as the probe was translated away from the edge of the acrylic slab. This suggests that the fringing effects are minimal and that the field lines extending beyond the electrode array do not significantly influence the estimated conductivity distribution bounded by the array. The AOS is therefore assumed to be the area enclosed by the electrodes only, 9.1 $mm^2 (= \pi r^2_{elect})$.

B. Gelatin Phantoms

Conductivity images of the high contrast metal wire embedded in a gelatin substrate are shown in Fig. 5. Because the probe was positioned by hand (to better simulate actual system deployment), it was challenging to precisely identify the wire location with respect to the

probe's electrode array. The images were therefore qualitatively evaluated; more quantitative metrics (i.e., using GREIT parameters [32]) might be appropriate for a more controlled experimental configuration. A high conductivity circular region, representing the metallic inclusion, is correctly localized at both the 3 o'clock and 9 o'clock positions. Similar to the saline tank experiments, a peripheral ring of low conductivity, associated with the 2-D FEM algorithm employed, is present around the circumference of the conductivity images. The blank gelatin image shows a more heterogeneous conductivity distribution than the saline images of Fig. 4; this heterogeneity is likely due to the inherent heterogeneity of the gelatin substrate, potentially stemming from small air bubbles and nonuniform mixing and setting of the gelatin within the small volume of the imaging domain. In addition, the electrode artifacts are not as uniform as the saline images; this likely arises from nonuniform electrode–gelatin interface for each of the electrodes. The probe was held in place by hand, which may result in nonuniform pressures being applied to each electrode.

C. Ex Vivo Porcine Imaging

The EIT probe was able to accurately differentiate muscle and adipose tissue in a porcine sample (see Fig. 6). The probe was straddled across a muscle/adipose tissue boundary; the resultant conductivity image depicts a two-region distribution with one half having a high conductivity (muscle) and the second half having a low conductivity (adipose). The probe was rotated 180° and the same region was imaged to confirm that images were independent of probe orientation. Fig. 7 shows discrete conductivity images acquired at the nine acquisition frequencies for one of the probe orientations. There is a clear separation between the muscle and adipose regions.

A semicircular region of interest (ROI) was selected within each half of the conductivity image (separating muscle and adipose regions) and the nodal conductivity values were averaged within each ROI (see Fig. 8). The ROIs were chosen to exclude peripheral nodes located within the outer 0.3 mm rim of each half of the image (~10% of the probe diameter); these regions are more prone to electrode artifacts (i.e., the low conductivity artifacts at 11:00 and 1:00 present in the conductivity images in Fig. 7). In addition, because the region between the two tissue types has a relatively slow conductivity gradient (due to the diffuse nature of EIT), and not the sharp step actually present between the muscle and adipose tissue, a 0.3-mm separation was included between the two ROIs so that the average conductivity computed within each ROI did not include the transition zone. These averages were computed and plotted for each of the nine frequencies scanned (see Fig. 8). The adipose tissue half of the image had a significantly lower conductivity ($p < 0.001$) than the muscle half did for all frequencies. The reconstructed conductivity values for muscle were ~0.15 S/m from 10 kHz–183 kHz. The adipose conductivity was ~0.015 S/m over this same frequency range. The large standard deviations (~33% and ~100% of the mean conductivity for the muscle and adipose regions, respectively) arise from the remaining peripheral regions of low conductivity surrounding the muscle tissue and peripheral regions of high conductivity surrounding the adipose tissue. These variations are due to the inaccuracy of the 2-D reconstruction algorithms employed and the point-spread function associated with EIT image reconstruction. Despite these artifacts, there is a significant separation between the high-contrast tissues.

Conductivity images of a small streak of adipose tissue embedded within muscle are shown in Fig. 9. The conductivity images clearly show a low conductivity region (adipose) straddled between two high conductivity regions (muscle). The width of the adipose streak measured via digital calipers at the center of the specimen was 0.46 mm, while the reconstructed stripe of low conductivity was 0.36 mm at the same central location.

IV. Discussion

There exists a strong clinical need for real-time intraoperative assessment of surgical margin status during cancer resections. The only approach currently in use to rapidly evaluate margin status during surgery is through microscopic assessment of intraoperative frozen sections (IFS) [33], [34]. In these cases, the tissue is removed from the body, flash frozen, histochemically stained, and microscopically evaluated by a pathologist. There are two primary challenges to using IFS assessment during robot-assisted laparoscopic prostatectomy (RALP). First, gaining access to the prostate tissue during a RALP is challenging. The prostate is typically resected, bagged, and placed within the pelvic space created through insufflation of the abdomen while the bladder neck / urethral anastomosis is completed (~30–60 min). Removing the prostate prior to the anastomosis would require dedocking of the robot and removal of one of the access ports, which would increase the overall operating time. Second, the surgeon would be required to mentally register the margin identified as positive on the IFS specimen to the tissues remaining within the body. This mental mapping is challenging, especially for small positive surgical margins.

The microendoscopic EIT probe developed here has the potential to overcome both of these clinical challenges. This probe is able to image at a near-millimeter resolution (i.e., Fig. 9), which is needed for identifying small islands of tumor cells left behind following tissue resection. Further, this probe was specifically designed to interface to the patient through small laparoscopic ports (<12 mm diameter), which will enable it to gauge tissues intraoperatively. Because this will be used to interface directly with the marginal tissue remaining within the body following tissue resection, the surgeon will not need to mentally register where a positive surgical margin is. Instead, the conductivity maps computed directly at the probe tissue interface will be displayed for the surgeon in real-time.

Fig. 10 shows an early prototype of the probe being manipulated during a RALP procedure under an Institutional Review Board approved protocol. This protocol permitted use of a passive probe to evaluate how the surgeon would manipulate the robotic forceps to interface with the silicone tube housing. The probe was successfully introduced through a 12-mm auxiliary surgical port and manipulated by the surgeon through use of the robotic forceps. This particular probe had the electrodes embedded within the probe tip, but the probe was not interfaced to an EIT system for voltage and current acquisition. Instead, this passive devise was used to demonstrate that the probe could easily be manipulated by the surgical instruments in preparation for future *in vivo* deployment. The two images show the left and right view screens that the surgeon sees during the procedure; these images are extracted from the dual-camera stereoendoscope used to provide a surgeon with a 3-D field of view. We anticipate overlaying EIT images directly onto the left and right view ports of the

surgeon's field of view to show directly on the tissue, and in 3D, where positive surgical margins might exist.

The only other previous attempt to construct an EIT-based “endotomography” device consisted of a 50-mm diameter cylindrical form (too large for clinical applications) with line electrodes embedded around the periphery of the cylinder (not effective for probing tissue surfaces) [35], [36]; this device was envisioned as being used for urethral introduction. Our device overcomes the limitations of this device for use in laparoscopic-based surgeries by being less than 12 mm in diameter (enabling it to fit through standard laparoscopic ports) and having surface electrodes embedded at the end of the probe (see Fig. 2). A second device recently reported for use in gynecological applications consists of a 48-electrode 30-mm diameter probe that the authors propose to introduce through the vaginal canal [37]. They showed images of 6-mm diameter inclusions in phantom studies. The device described here has a smaller diameter than this gynecological probe and we have demonstrated submillimeter image resolution. Other small form-factor impedance sensing probes have also been developed for evaluating tissue anisotropy [38]–[40], but have not been specifically designed for use in evaluating surgical margins during robotic surgical procedures.

The 2-D reconstruction algorithms used here result in boundary artifacts clearly shown in the saline tank, gelatin, and porcine experiments (see Figs. 4 and 5). The nonuniform conductivity distribution is a well-documented artifact that arises when assuming a 2-D geometry in a 3-D experimental configuration [31]. Three-dimensional reconstruction algorithms are becoming the standard for EIT [30] and should be considered for this application going forward. One benefit of using 2-D algorithms is speed of image reconstruction; 2-D algorithms can be used to produce images on the order of milliseconds on a standard laptop/desktop computer, while 3-D algorithms typically require multiple minutes depending on the mesh density used. In terms of clinical deployment, it is critical that surgeons be given near-immediate feedback regarding margin pathology. Speed optimized 3-D reconstruction algorithms based on precomputing the Jacobian or using novel algorithms implemented for instance on graphical processor units should be considered for clinically deploying this probe [41].

The significant drop in conductivity associated with increasing frequency [see Fig. 4(b)] is due to parasitic impedances associated with the cable length of the probe. This limits the spectral range that can be used to interrogate the tissue. This spectral information is potentially important for enhancing the sensitivity and specificity of EIT as discussed below. *Ex vivo* studies have shown that spectral impedance properties are more sensitive and specific than discrete frequencies alone [21]. One approach to improving the spectral range of the probe would be to consider using active electronics located near to the probe tip similar to [42].

While the conductivity contrast between muscle (15–40 mS/m) [43] and adipose (2 mS/m) [44] tissue exceeds that typically found between benign and malignant prostate, these findings suggest that imaging biological tissue samples is possible. The conductivity of malignant prostate ranges from 90 mS/m–140 mS/m over the frequency range of 100 Hz–

100 kHz, which is significantly lower than the conductivity of fibromuscular stroma (119 mS/m–150 mS/m) and significantly higher than adipose (~2 mS/m) over the same frequency range [20]; fibromuscular stroma and adipose tissues are the primary tissue types making up the peri-prostatic region which would be probed following prostate resection. Other electrical properties measured from *ex vivo* human prostate samples have exhibited even higher contrast than conductivity alone. The mean permittivity of cancer was reported to be 2.7 times larger than that of stromal tissues (30.3 mS/m versus 11.2 mS/m) at 100 kHz [20]. Likewise, Cole-based spectral parameters including the high frequency conductivity (σ_∞), high-to-low frequency conductivity difference ($\Delta\sigma$), and the characteristic frequency (f_c) have all been reported to provide high levels of contrast approaching 1.6, 3.0, and 5.1, respectively [21]. Further studies exploring a broad range of frequencies and these additional electrical properties with *ex vivo* and *in vivo* prostate tissue are needed to verify that small islands of cancer cells can be visualized with this probe.

Based on these previous reports of *ex vivo* prostate tissue, it is expected that imaging permittivity or spectral impedance parameters will provide even greater contrast than with conductivity alone [20], [21]. One challenge to spectral parameter imaging would be acquiring a wider band of frequencies (>200 kHz). The parasitic impedances associated with the probe's long form factor (~55 cm) make high frequency data acquisition challenging [see, for example, the conductivity traces for 263 and 545 kHz in Fig. 4(b)]. One might consider using a tissue-based calibration in which the probe is calibrated with respect to known tissue types (i.e., benign versus malignant) at high frequencies. Alternatively, use of active electrodes might be a novel way to enable wider band acquisition; however, instrumenting the probe with the additional amplifiers required would be difficult given the imposed space constraints. Extending the probe to higher frequencies is an area of active research.

Other competing endoscopic technologies are being explored for use in surgical margin assessment. These technologies are primarily optical-based approaches and include fiber-optic microscopy of fluorescent tracers [45], optical coherence tomography [46], two-photon excited autofluorescence microscopy [47], Raman spectroscopy [48], and coherent antiStokes Raman scattering microscopy [49]. The majority of these technologies [45], [47] are being used for identifying the neurovascular bundles during nerve-sparing procedures. The Raman scattering based approaches [48], [49] are also attempting to distinguish benign from malignant tissues at the surgical margins. These technologies are still in development, so precise measures of sensitivity and specificity to surgical margin status are still undetermined. Going forward, a synergistic approach coupling a fiber-bundle within the center of our electrode array might be considered. Leveraging both the optical and electrical properties in a multimodal device such as this may improve sensitivity and specificity of surgical margin assessment.

V. Conclusion

To the best of our knowledge, this represents the first EIT device developed for endoscopic applications that is able to image submillimeter features within biological tissues. Specifically, a small form factor flexible endoscopic EIT probe has been successfully

developed for use in RALP. This probe is able to accurately sense electrical properties up to a bandwidth of 183 kHz. The probe is able to sense subsurface impedance changes down to a depth of ~1.5 mm and is able to image structures smaller than 0.5 mm in width within a 9.1 mm^2 circular field of view. The probe can easily be grasped and manipulated with most laparoscopic forceps. Additional testing on human tissues is required to evaluate the efficacy of using electrical impedance imaging for intraoperative surgical margin assessment during RALP procedures.

Acknowledgments

This work was supported in part by the U.S. National Institutes of Health under Grant 1R01CA143020–01A1 and Intuitive Surgical, Inc.

References

1. Siegel R, Ma J, Zou Z, Jemal A. Cancer statistics, 2014. CA: A Cancer J. Clinicians. 2014; 64:9–29.
2. Anast JW, Andriole GL, Bismar TA, Yan Y, Humphrey PA. Relating biopsy and clinical variables to radical prostatectomy findings: Can insignificant and advanced prostate cancer be predicted in screening population? Urology. 2004; 64:544–550. [PubMed: 15351590]
3. CDC/NCHS National Hospital Discharge Survey. 2010. [Online]. Available: http://www.cdc.gov/nchs/data/nhds/4procedures/2010pro4_numberrate.pdf
4. Brooks, JD. Anatomy of the lower urinary tract and male genitalia. In: Wein, A., editor. Campbell's Urology. 9th ed.. Saunders Elsevier; Philadelphia, PA, USA: 2007.
5. Roehl KA, Han M, Ramos CG, Antenor JAV, Catalona WJ. Cancer progression and survival rates following anatomical radical retropubic prostatectomy in 3,478 consecutive patients: Long-term results. J. Urol. 2004; 172:910–914. [PubMed: 15310996]
6. Orvieto MA, Alsikafi NF, Shalhav AL, Laven BA, Steinberg GD, Zagaja GP, Brendler CB. Impact of surgical margin status on long-term cancer control after radical prostatectomy. BJU Int. 2006; 98:1199–1203. [PubMed: 17125478]
7. Karakiewica PI, Eastham JA, Graefen M, Cagiannos I, Stricker PD, Klein E, Cangiano T, Schroder FH, Scardino PT, Kattan MW. Prognostic impact of positive surgical margins in surgically treated prostate cancer: Multi-institutional assessment of 5831 patients. Urology. 2005; 66:1245–1250. [PubMed: 16360451]
8. Brown B, et al. Relation between tissue structure and imposed electrical current flow in cervical neoplasia. Lancet. 2000; 355:892–895. [PubMed: 10752706]
9. Abdul A, Brown B, Milnes P, Tidy JA. A clinical study of the use of impedance spectroscopy in the detection of cervical intraepithelial neoplasia (CIN). Gynecologic Oncology. 2005; 99:S64–S66. [PubMed: 16450430]
10. Brown B, Milnes P, Abdul A, Tidy JA. Detection of cervical intraepithelial neoplasia using impedance spectroscopy: a prospective study. Brit. J. Obstetrics Gynaecology. 2005; 112:802–806.
11. Abdul A, Brown B, Milnes P, Tidy J. The use of electrical impedance spectroscopy in the detection of cervical intraepithelial neoplasia. Int. J. Gynecol Cancer. 2006; 16:1823–1832. [PubMed: 17009978]
12. Jossinet J. Variability of impedivity in normal and pathological breast tissue. Med. Biol. Eng. Comput. 1996; 34:346–350. [PubMed: 8945857]
13. Surowiec A, Stuchly A, Barr JR, Swarup A. Dielectric properties of breast carcinoma and the surrounding tissues. IEEE Trans. Biomed. Eng. Apr.1988 35(4):257–263. [PubMed: 2834285]
14. Zou Y, Guo Z. A review of electrical impedance techniques for breast cancer detection. Med. Eng. Phys. 2003; 25:79–90. [PubMed: 12538062]

15. Åberg P, Nicander I, Hansson J, Geladi P, Holmgren U, Ollmar S. Skin cancer identification using multifrequency electrical impedance—a potential screening tool. IEEE Trans. Biomed. Eng. Dec. 2004 51(12):2097–2102. [PubMed: 15605856]
16. Aberg P, Geladi P, Nicander I, Hansson J, Holmgren U, Ollmar S. Non-invasive and microinvasive electrical impedance spectra of skin cancer—a comparison between two techniques. Skin Res. Technol. 2005; 11:281–286. [PubMed: 16221145]
17. Wilkinson B, Smallwood RH, Keshtar A, Lee JA, Hamdy FC. Electrical impedance spectroscopy and the diagnosis of bladder pathology: A pilot study. J. Urol. 2002; 168:1563–1567. [PubMed: 12352458]
18. Keshtkar A, Keshtkar A, Smallwood R. Electrical impedance spectroscopy and the diagnosis of bladder pathology. Physiol. Meas. 2006; 27:585–596. [PubMed: 16705257]
19. Halter RJ, Schned A, Heaney J, Hartov A, Schutz S, Paulsen KD. Electrical impedance spectroscopy of benign and malignant prostatic tissues. J. Urol. 2008; 179:1580–1586. [PubMed: 18295258]
20. Halter RJ, Schned A, Heaney J, Hartov A, Paulsen KD. Electrical properties of prostatic tissues: I. Single frequency admittivity properties. J. Urol. 2009; 182:1600–1607. [PubMed: 19683745]
21. Halter RJ, Schned A, Heaney J, Hartov A, Paulsen KD. Electrical properties of prostatic tissues: II. Spectral admittivity properties. J. Urol. 2009; 182:1608–1613. [PubMed: 19683743]
22. Halter RJ, Hartov A, Heaney J, Paulsen KD, Schned A. Electrical impedance spectroscopy of the human prostate. IEEE Trans. Biomed. Eng. Jul.2007 54(7):1321–1327. [PubMed: 17605363]
23. Cole KS, Cole RH. Dispersion and absorption in dielectrics: I. Alternating current characteristics. J. Chem. Phys. 1941; 9:341.
24. Halter RJ, Hartov A, Paulsen KD. A broadband high frequency electrical impedance tomography system for breast imaging. IEEE Trans. Biomed. Eng. Feb.2008 55(2):650–659. [PubMed: 18270001]
25. Cheney M, Isaacson D. Distinguishability in impedance imaging. IEEE Trans. Biomed. Eng. Aug. 1992 39(8):852–860. [PubMed: 1505998]
26. Holder, DS. Electrical Impedance Tomography: Methods, History and Applications. CRC Press; Boca Raton, FL, USA: 2004.
27. Paulsen KD, Moskowitz K, Ryan T. Temperature field estimation using electrical impedance profiling methods: 1. Reconstruction algorithm and simulated results. Int. J. Hyperthermia. 1994; 10:209–228. [PubMed: 8064181]
28. Cheng KS, Isaacson D, Newell JC, GIsser DG. Electrode models for electric current computed tomography. IEEE Trans. Biomed. Eng. Sep.1989 36(9):918–924. [PubMed: 2777280]
29. Vauhkonen PJ, Vauhkonen M, Savolainen T, Kaipio JP. Three-dimensional electrical impedance tomography based on the complete electrode model. IEEE Trans. Biomed. Eng. Sep.1999 46(9): 1150–1160. [PubMed: 10493078]
30. Borsic A, Hartov A, Paulsen KD, Manwaring P. 3D electric impedance tomography reconstruction on multi-core computing platforms. Proc. IEEE 30th Annu. Int. Conf. Eng. Med. Biol. Soc. 2008:1175–1177.
31. Halter RJ, Hartov A, Paulsen KD. Experimental justification for using 3D conductivity reconstructions in electrical impedance tomography. Physiol. Meas. 2007; 28:S115–S127. [PubMed: 17664629]
32. Adler A, Arnold JH, Bayford R, Borsic A, Brown B, Dixon P, Faes TJC, Frerichs I, Gagnon H, Garber Y, Grychtol B, Hahn G, Lionheart WRB, Malik A, Patterson RP, Stocks J, Tizzard A, Weiler N, Wolf GK. GREIT: a unified approach to 2D linear EIT reconstruction of lung images. Physiol. Meas. 2009; 30:S35–S55. [PubMed: 19491438]
33. Lepor H, Kaci L. Role of intraoperative biopsies during radical retropubic prostatectomy. Urology. 2004; 63:499–502. [PubMed: 15028445]
34. Dillenburg W, Poulakis V, Witzsch U, De Vries R, Skriapas K, Altmansberger H, Becht E. Laparoscopic radical prostatectomy: The value of intraoperative frozen sections. Eur. Urol. 2005; 48:614–621. [PubMed: 16054291]
35. Jossinet J, Fournier-Desseux A, Matias A. Assessment of electrical impedance endotomography for hardware specification. Biomed. Imag. Intervention. 2006; 2:1–15.

36. Jossinet J, Marry E, Matias A. Electrical impedance endotomography. Phys. Med. Biol. 2002; 47:2189–2202. [PubMed: 12164581]
37. Cherepenin VA, Gulyaev YV, Korjenevsky AV, Sapetsky SA, Tuykin TS. An electrical impedance tomography system for gynecological application GIT with a tiny electrode array. Physiol. Meas. 2012; 33:849–862. [PubMed: 22531280]
38. Steendijk P, Mur G, Van Der Velde ET, Baan J. The four-electrode resistivity technique in anisotropic media: theoretical analysis and application on myocardial tissue *in vivo*. IEEE Trans. Biomed. Eng. Nov.1993 40(11):1138–1148. [PubMed: 8307598]
39. Kwon H, Wi H, Karki B, Lee EJ, McEwan A, Woo EJ, Harrach B, Seo JK, Oh TI. Bioimpedance spectroscopy tensor probe for anisotropic measurements. Electron. Lett. 2012; 48:1253–1255.
40. Huo X, Shi X, You F, Fu F, Liu R, Tang C, Lu Q, Dong X. Reliability of *in vivo* measurements of the dielectric properties of anisotropic tissue: a simulative study. Phys. Med. Biol. 2013; 58:3163–3176. [PubMed: 23603795]
41. Borsic A, Attardo EA, Halter RJ. Multi-GPU Jacobian accelerated computing for soft-field tomography. Physiol. Meas. 2012; 33:1703–1715. [PubMed: 23010857]
42. Li JH, Joppek C, Faust U. Fast EIT data acquisition system with active electrodes and its application to cardiac imaging. Physiol. Meas. 1996; 17:A25–A32. [PubMed: 9001599]
43. Faes TJC, van der Meij HA, de Munck JC, Heethaar RM. The electric resistivity of human tissues (100 Hz–10 MHz): A meta-analysis of review studies. Physiol. Meas. 1999; 20:R1–R10. [PubMed: 10593226]
44. Gabriel S, Lau RW, Gabriel C. The dielectric properties of biological tissues: II. Measurements in the frequency range 10 Hz to 20 GHz. Phys. Med. Biol. 1996; 41:2251–2269. [PubMed: 8938025]
45. Boyette LB, Reardon MA, Mirelman AJ, Kirkley TD, Lysiak JJ, Tuttle JB, Steers WD. Fiberoptic imaging of cavernous nerves *in vivo*. J. Urol. 2007; 178:2694–2700. [PubMed: 17945279]
46. Rais-Bahrami S, Levinson AW, Fried NM, Lagoda GA, Hristov A, Chuang Y, Burnett AL, Su LM. Optical coherence tomography of cavernous nerves: A step toward real-time intraoperative imaging during nerve-sparing radical prostatectomy. Urology. 2008; 72:198–204. [PubMed: 18280549]
47. Yadav R, Mukherjee S, Hermen M, Tan G, Maxfield FR, Webb WW, Tewari AK. Multiphoton microscopy of prostate and periprostatic neural tissue: A promising imaging technique for improving nerve-sparing prostatectomy. J. Endourology. 2009; 23:861–867.
48. Hanchanale VS, Rao AR, Das S. Raman spectroscopy and its urological applications. Indian J. Urol.: J. Urol. Soc. India. 2008; 24:444–450.
49. Gao L, Zhou H, Thrall MJ, Li F, Yang Y, Wang Z, Wong ST. Label-free high-resolution imaging of prostate glands and cavernous nerves using coherent anti-Stokes Raman scattering microscopy. Biomed. Opt. Exp. 2011; 2:915–926.

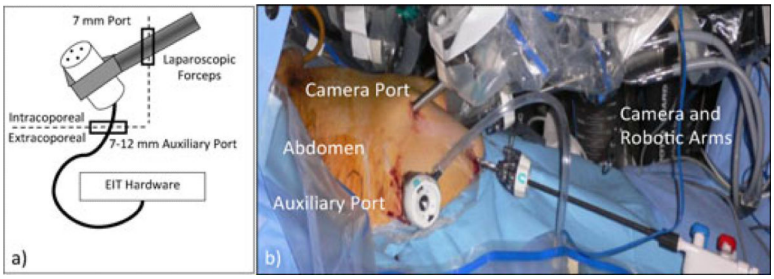

Fig. 1.

a) Conceptualized configuration of how a microendoscopic EIT probe will be incorporated into a laparoscopic procedure. Multiple port sizes (7–12 mm) are often available for laparoscopic procedures depending on what laparoscopic tools are required for a specific procedure. b) Abdominal surgical environment and port placement during a RALP. The EIT probe would be introduced through the 12-mm diameter auxiliary port. Image acquired from a RALP procedure at Dartmouth–Hitchcock Medical Center.

Fig. 2.

a) Schematic and dimensions of designed microendoscopic EIT probe tip. The edge-to-edge electrode array radius, r_{elect} , used for computing area of sensitivity is 1.7 mm (distance from probe center to edge of electrode = 1.4 mm + 0.3 mm). b) View of active surface of EIT probe. The electrodes are gold-plated and embedded in a polyethylene housing of 5 mm in diameter. c) The entire housing and electrode cables are embedded within a 55 cm long, 7 mm diameter silicone tube. Scale in cm.

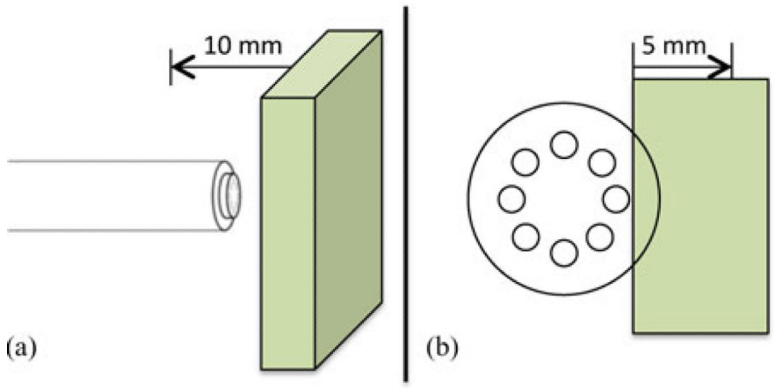

Fig. 3.

a) Schematic view of the MDOS experiment. b) Schematic view of the AOS experiment. An acrylic slab was used as the high impedance structure.

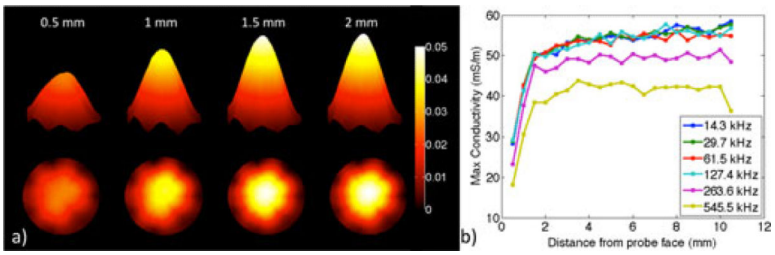

Fig. 4.

(a) Conductivity images of saline recorded as EIT-SMA probe is translated away from a high impedance acrylic interface at distances of 0.5 mm, 1 mm, 1.5 mm, and 2 mm; frequency of operation is 127 kHz. The top row shows the surface map for each location, while the second row shows the 2-D enface view. b) Maximum conductivity computed as a function of distance as probe is translated away from insulating inclusion for different signal frequencies. Note that conductivity images and the maximum conductivity traces in (b) demonstrate a maximum depth of sensitive (MDOS) to approximately 1.5 mm. Additional high frequency data (263.6 kHz and 545.5 kHz) data is included to show how the unaccounted for parasitic impedances of the long probe influence reconstructed conductivities.

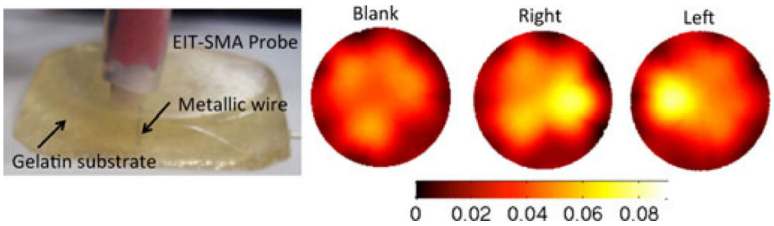

Fig. 5.

Experimental configuration for gelatin experiments (left). Conductivity images generated when the probe was positioned on a gelatin-only region of the phantom, positioned such that the metal inclusions was at the 3 o'clock position, and at the 9 o'clock position (right). Yellow denotes high conductivity associated with the metal inclusion. Color bar in units of S/m.

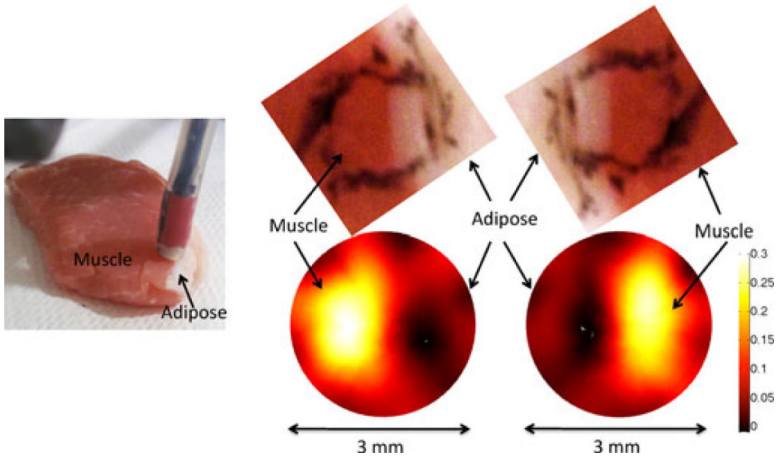

Fig. 6.

Experimental configuration for the two-tissue (muscle, adipose) porcine EIT-SMA probing procedure (left). Black ink was used to identify where the probe was positioned. The probe was rotated 180° to demonstrate rotational invariance. Conductivity images for the two angular positions are shown on the bottom right. The adipose tissue shows up as a low conductivity, while the muscle tissue exhibits higher conductivities. Color bar in units of S/m.

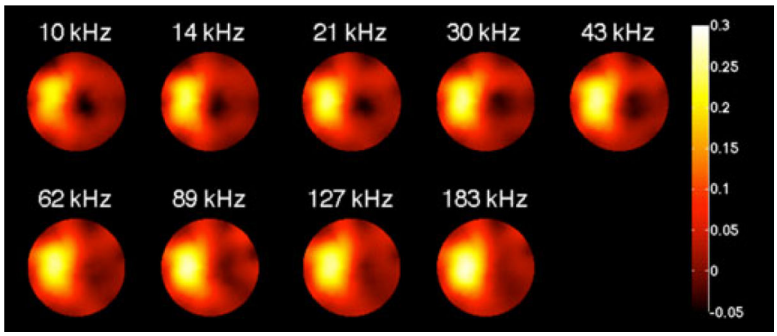

Fig. 7.

Conductivity images of two-tissue porcine sample at nine logarithmically spaced frequencies ranging from 10 to 183 kHz. Muscle is on the left of each image (yellow) and adipose is on the right (dark orange/black). Color bar in units of S/m.

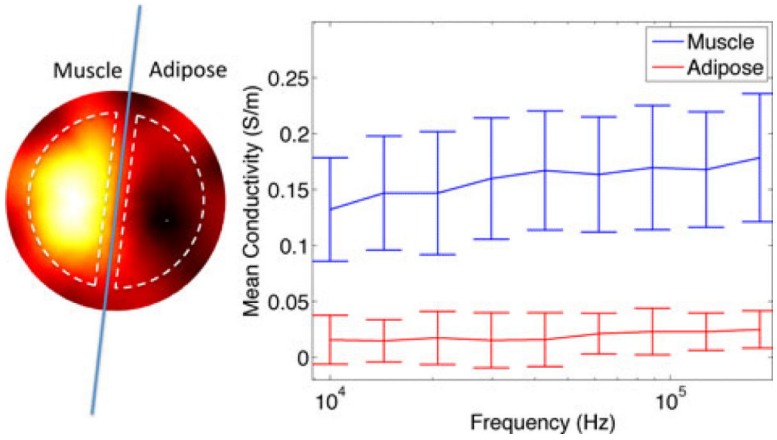

Fig. 8.

Conductivity images were subdivided into adipose and muscle tissue ROIs (left). The mean conductivity within each ROI (dashed lines) was computed and plotted as function of frequency (right). Error bars represent standard deviation of nodal conductivity values computed from each tissue type.

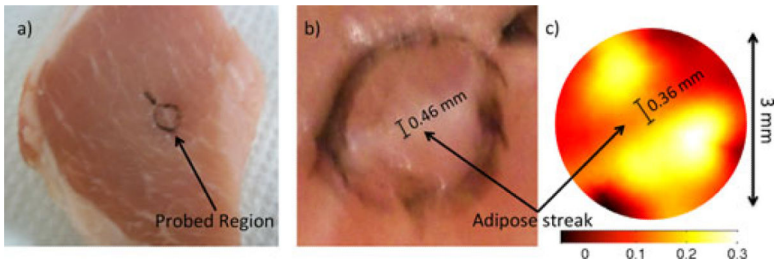

Fig. 9.

a) Experimental conditions for imaging small features in *ex vivo* porcine tissue. A black circle denotes the region probed; the straight line identifies where electrode 1 was positioned. b) A magnified view of region probed. A thin <1 mm thick streak of adipose tissue (white) is located between two muscular tissue regions (pink). The image in B has been rotated with respect to the image in A to align with the correct probe orientation used for the FEM mesh (C). c) Conductivity image of the probed region shows a low conductivity streak associated with the adipose streak surrounded by two higher conductivity muscular regions. Color bar in units of S/m.

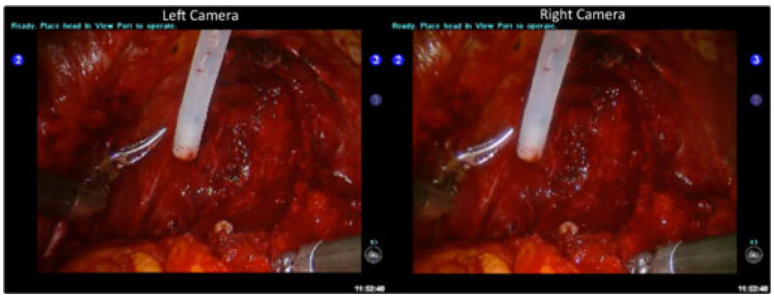

Fig. 10.

Left and right camera views recorded from the surgical console of a da Vinci Surgical System. Images recorded during a RALP procedure. An early prototype EIT-SMA probe was being manipulated by the surgical forceps (not seen) and pressed into the periprostatic tissue bed after the prostate has been fully resected.